





# First High-resolution Spectroscopy of X-Ray Absorption Lines in the Obscured State of NGC 5548

Missagh Mehdipour<sup>1</sup> , Gerard A. Kriss<sup>1</sup> , Jelle S. Kaastra<sup>2,3</sup> , Elisa Costantini<sup>2,4</sup> , Liyi Gu<sup>2,3,5</sup> , Hermine Landt<sup>6</sup> , Junjie Mao<sup>2,7</sup> , and Daniele Rogantini<sup>8,9</sup> 

<sup>1</sup> Space Telescope Science Institute, 3700 San Martin Drive, Baltimore, MD 21218, USA; [mmehdipour@stsci.edu](mailto:mmehdipour@stsci.edu)

<sup>2</sup> SRON Netherlands Institute for Space Research, Niels Bohrweg 4, 2333 CA Leiden, The Netherlands

<sup>3</sup> Leiden Observatory, Leiden University, P.O. Box 9513, 2300 RA Leiden, The Netherlands

<sup>4</sup> Anton Pannekoek Institute, University of Amsterdam, Postbus 94249, 1090 GE Amsterdam, The Netherlands

<sup>5</sup> RIKEN High Energy Astrophysics Laboratory, 2-1 Hirosawa, Wako, Saitama 351-0198, Japan

<sup>6</sup> Centre for Extragalactic Astronomy, Department of Physics, Durham University, South Road, Durham DH1 3LE, UK

<sup>7</sup> Department of Astronomy, Tsinghua University, Haidian DS 100084, Beijing, People's Republic of China

<sup>8</sup> Department of Astronomy and Astrophysics, University of Chicago, Chicago, IL 60637, USA

<sup>9</sup> MIT Kavli Institute for Astrophysics and Space Research, Massachusetts Institute of Technology, Cambridge, MA 02139, USA

Received 2023 December 5; revised 2024 January 4; accepted 2024 January 5; published 2024 February 15

## Abstract

Multiwavelength spectroscopy of NGC 5548 revealed remarkable changes due to the presence of an obscuring wind from the accretion disk. This broadened our understanding of obscuration and outflows in active galactic nuclei. Swift monitoring of NGC 5548 shows that over the last 10 yr, the obscuration has gradually declined. This provides a valuable opportunity for analyses that have not been feasible before because of too much obscuration. The lowered obscuration, together with the high-energy spectral coverage of Chandra HETG, facilitates the first study of X-ray absorption lines in the obscured state. The comparison of the lines (Mg XI, Mg XII, Si XIII, and Si XIV) between the new and historical spectra reveals interesting changes, most notably the He-like absorption being significantly diminished in 2022. Our study finds that the changes are caused by an increase in both the ionization parameter and the column density of the warm-absorber outflow in the obscured state. This is contrary to the shielding scenario that is evident in the appearance of the UV lines, where the inner obscuring wind shields outflows that are farther out, thus lowering their ionization. The X-ray absorption lines in the HETG spectra appear to be unaffected by the obscuration. The results suggest that the shielding is complex because various components of the ionized outflow are affected differently. We explore various possibilities for the variability behavior of the X-ray absorption lines and find that the orbital motion of a clumpy ionized outflow traversing our line of sight is the most likely explanation.

*Unified Astronomy Thesaurus concepts:* X-ray active galactic nuclei (2035); Seyfert galaxies (1447); Quasar absorption line spectroscopy (1317); High resolution spectroscopy (2096)

## 1. Introduction

Understanding the co-evolution of active galactic nuclei (AGN) and their host galaxies has been one of the major endeavors of modern astronomy. AGN activity in the nucleus and star formation in the surrounding interstellar medium are thought to influence each other via a feedback mechanism (Silk & Rees 1998; King & Pounds 2015; Gaspari & Sądowski 2017; Harrison et al. 2018). AGN outflows/winds likely play a significant role, as they serve as conduits of mass and energy into the host galaxy environment. To this end, finding out the uncertain properties of these outflows is important for assessing their contribution to AGN feedback.

The dynamics, kinematics, and ionization structure of ionized outflows, extending from the vicinity of the accretion disk to the outskirts of the host galaxy, are not well understood. This makes it challenging to ascertain how their momentum and energy propagate into the galaxy, and how they affect their environment. Different types/forms of ionized outflows, with distinct characteristics, have been observed at the micro (sub-pc) scale (disk and the broad-line region, BLR), the meso (pc)

scale (the torus and the narrow-line region, NLR), and the macro (kpc) scale (the host galaxy environment); see e.g., Gaspari et al. (2020), Laha et al. (2021). The formation of these various ionized outflows and their association to one another are uncertain. The origin (disk or torus) and the launch and driving mechanism (thermal, radiative, or magnetic) of the ionized outflows remain open questions. Currently it is not well established what physical factors govern the launch and duty cycle of these winds.

The obscuring disk wind (obscurer) that was first discovered in NGC 5548 (Kaastra et al. 2014; Arav et al. 2015) is significantly faster and more massive than the moderate ionized outflows (also called warm absorbers). Whereas warm absorbers typically reside at pc-scale distances in the NLR, the obscurer is at distances of light-days from the black hole, extending to and beyond the BLR. Such obscuring winds are transient and highly variable, and partially cover the central X-ray source (Di Gesu et al. 2015; Mehdipour et al. 2016b; Cappi et al. 2016). Apart from NGC 5548, they have been found in several other AGN, including Mrk 335 (Longinotti et al. 2013), NGC 985 (Ebrero et al. 2016a), NGC 3783 (Mehdipour et al. 2017), NGC 3227 (Mehdipour et al. 2021), Mrk 817 (Kara et al. 2021), PG 1114 + 445 (Serafinelli et al. 2021), and MR 2251-178 (Mao et al. 2022). Joint X-ray and UV spectroscopy has been instrumental in probing the nature

of these obscuring winds. The appearance of broad and blueshifted UV absorption lines alongside X-ray obscuration in some objects suggests a link between these phenomena and enables the kinematics of the obscurer to be ascertained.

The Hubble Space Telescope (HST) Cosmic Origins Spectrograph (COS) spectroscopy of NGC 5548 suggests that the ionized outflows are shielded from the X-ray source by the obscurer, causing them to become less ionized (Arav et al. 2015; Kriss et al. 2019). This is seen by the detection of new low-ionization narrow absorption lines in the UV, such as C II and Si II (Arav et al. 2015; Mehdipour et al. 2022). This scenario is also supported by the infrared spectroscopy of He I (Wildy et al. 2021) and the appearance of broad wings on some of the coronal emission lines (Kynoch et al. 2022). Interestingly, obscuration in NGC 5548 is likely present in all directions, which would explain peculiar periods of de-correlation between the variabilities of the continuum and the BLR emission lines (Dehghanian et al. 2019a). Therefore, such global obscuration/shielding affects our interpretation of both the ionized outflows (Dehghanian et al. 2019b) and the reverberation mapping of the BLR (Dehghanian et al. 2019a). Interestingly, shielding from the ionizing X-ray source is thought to be required to prevent over-ionization of the UV-absorbing gas and thus allow radiative driving (Proga & Kallman 2004). However, the need for this X-ray shielding in radiation-driven winds remains an open area of research in the literature (e.g., Higginbottom et al. 2014).

Recently in Mehdipour et al. (2022), hereafter M22, we reported on the striking long-term variability of the obscuring disk wind based on HST and Swift monitoring data (see Figures 1 and 2 in M22). The Swift/X-Ray Telescope (XRT) hardness ratio is a useful tracer of the strength of X-ray obscuration. Swift showed that the X-ray spectral hardening in NGC 5548 as a result of obscuration has declined over the years, reaching its lowest in 2022. At this point we found the broad C IV UV absorption significantly weakened, while the broad Ly $\alpha$  absorption was still significantly present. The associated narrow low-ionization UV absorption lines, produced previously by the warm absorber when shielded from the X-rays, were also remarkably diminished in 2022. We found a highly significant correlation between the variabilities of the X-ray spectral hardening and the equivalent width of the broad C IV absorption line, demonstrating that the X-ray obscuration is inherently linked to disk winds (M22).

The lowered obscuration, and hence the higher signal-to-noise ratio (S/N) achieved with the brighter continuum, provides a new opportunity to study the X-ray absorption lines in the obscured state of NGC 5548. Here we present the high-resolution X-ray spectroscopy of the absorption lines with our new Chandra High Energy Transmission Grating (HETG) observations. This follows our study of the associated HST and Swift data in M22. The ionized outflows of NGC 5548 have been extensively studied in the historical unobscured epoch with high-resolution XMM-Newton and Chandra spectra (e.g., Kaastra et al. 2000; Steenbrugge et al. 2005; Kaastra et al. 2014; Ebrero et al. 2016b). The aim of this paper is thus not a full reanalysis of the ionized outflows, but rather to investigate any relative changes in them during the obscured epoch. This would help us better understand the relation between the obscurer and the ionized outflows, and ascertain the role and impact of shielding by the obscurer on the ionized outflows.

**Table 1**  
Log of Chandra/HETG Observations of NGC 5548 from Three Epochs

Obs. ID	Start Time	Exposure (ks)
3046	2002-01-16 06:12	151.4
21846	2019-05-05 14:58	29.7
22207	2019-06-18 13:16	50.3
21694	2019-08-09 03:04	60.5
22681	2019-08-10 22:39	27.2
25802	2021-12-30 01:54	21.7
26256	2021-12-30 15:16	21.7
25803	2021-12-31 05:34	27.6
25392	2022-01-30 18:31	24.7
25800	2022-01-31 08:33	29.6
25801	2022-01-31 22:18	19.8

**Note.** The individual HETG spectra from each epoch are combined into one spectrum for our modeling and are referred to as the “2002,” “2019,” and “2022” observations.

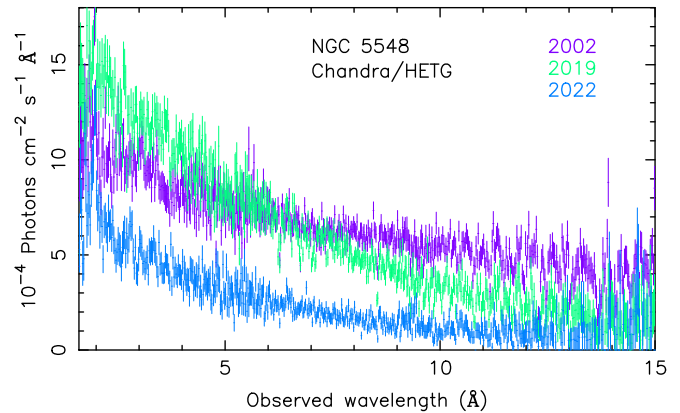


**Figure 1.** An overview of the new and historical HETG spectra of NGC 5548. The 2002 spectrum is from the unobscured epoch. The 2019 and 2022 spectra are both obscured, with the intrinsic continuum being brighter in 2019.

## 2. Observations and Data Processing

The log of the Chandra/HETG observations of NGC 5548 that we are studying here is provided in Table 1. These Chandra data are contained in DOI:10.25574/cdc.193. An overview of the HETG spectra from the three epochs is shown in Figure 1. Our most recent observation of NGC 5548 was approved in a joint Chandra Cycle 23 proposal, providing a 150 ks exposure with HETG and two orbits with HST/COS. To meet Chandra’s observing requirement, the observation was split, spanning 2021 December and 2022 January. For brevity we refer to this as the “2022” observation. Additionally, in 2019 a Guaranteed Time HETG observation with 175 ks exposure was obtained in the obscured epoch. To help us better understand these 2019 and 2022 obscured spectra, we make use of an unobscured observation from 2002 with 151 ks exposure. This 2002 observation was accompanied with a HST Space Telescope Imaging Spectrograph (STIS) observation. In this paper, we also make use of the 2013 HST/COS spectrum from the epoch of the strongest obscuration for comparison with other observations. The new and archival HST spectra of NGC 5548 have been described in our previous works (Kaastra et al. 2014; Arav et al. 2015; Kriss et al. 2019, M22). Here we focus on the description and analysis of the HETG spectra.

In all the HETG observations, the ACIS camera was operated in the timed exposure (TE) read mode and the FAINT data mode. The data were reduced using the Chandra Interactive Analysis of Observations (CIAO) v4.14 software. The `chandra_repro` script of CIAO and its associated tools were used for the reduction of the data and production of the final grating products: PHA2 spectra, Response Matrix Files, and Ancillary Response Files. The grating spectra and their associated response files were combined using the CIAO `combine_grating_spectra` script. The  $\pm$  first-order spectra of each grating were combined. In addition to producing a High Energy Grating (HEG) and Medium Energy Grating (MEG) spectrum for each observation, we also produced stacked HEG and MEG spectra containing all the data. We therefore produced three sets of spectra for our spectral modeling: 2002, 2019, and the 2022 spectra (Figure 1). The HETG spectra from each epoch display similar absorption features and are consistent with one another, thus allowing us to stack the spectra to enhance the S/N. In our spectral modeling, HEG and MEG spectra are fitted simultaneously. The fitted spectral range is 2.5–26 Å for MEG, and 1.55–14.5 Å for HEG. We take into account the instrumental flux difference between HEG and MEG by rescaling the normalization of HEG relative to MEG in our spectral modeling. Over these energy bands, the HEG/MEG flux ratio is 0.96 in 2002, 0.94 in 2019, and 0.95 in 2022.

### 3. Spectral Analysis and Modeling

We have carried out our spectral modeling using SPEX v3.07.01 (Kaastra et al. 1996, 2022). In our modeling, the cosmological redshift is set to 0.017175 (de Vaucouleurs et al. 1991) using `reds` in SPEX. The X-ray absorption by the Milky Way is modeled with the `hot` model with its temperature fixed to 0.001 eV and  $N_{\text{H}} = 1.45 \times 10^{20} \text{ cm}^{-2}$  (Wakker et al. 2011). The Galactic reddening is modeled using an `ebv` component with  $E(B - V) = 0.02$  (Schlegel et al. 1998) and  $R_V$  fixed to 3.1.

We modeled the HETG absorption lines with two different methods. In the first method, we fitted each line using the `slab` model. This allows the column density and velocity of an individual ion to be independently measured. In this approach, prior knowledge of the ionizing spectral energy distribution (SED) and the ionization state of the gas is not needed, hence providing a more model agnostic diagnosis of the lines and their variability. In the second method, we use photoionization modeling using the `pion` model (Miller et al. 2015; Mehdipour et al. 2016a). This model takes into account the ionizing SED and computes the ionization balance of the gas, and thus all ionic column densities are linked in a physically consistent fashion. In our computations of the photoionization equilibrium and the X-ray spectrum, the elemental abundances are fixed to the proto-solar values of Lodders et al. (2009).

To model the broadband continuum, we used the SED model that we previously established for NGC 5548 using our multiwavelength campaign (Mehdipour et al. 2015). In this model, the SED consists of three continuum components: `comt` for modeling the optical/UV disk emission and the soft X-ray excess with warm Comptonization `pow` for modeling the X-ray power law, and `refl` for modeling the X-ray reflection. The normalization and photon index of `pow` are fitted to the HETG spectra. The low-energy and high-energy exponential cutoffs of `pow` are fixed to 1 Ryd and 400 keV, respectively

(Mehdipour et al. 2015). We scale the normalization of the `comt` model to match the HST UV continuum level. The other parameters of `comt` are kept frozen to those obtained from the 2013 campaign (Mehdipour et al. 2015) because they cannot be constrained with HETG, mainly because of the loss of effective area in the soft band. Also, because of lack of any UV data for the 2019 observation, we set the normalization of its `comt` to that of the 2022 observation. The parameters of the illuminating power law for the `refl` component are coupled to those of the 2002 intrinsic power law, and the scale parameter of the `refl` model is freed to fit the Fe K $\alpha$  line.

Despite the gradual long-term decline of the obscurer, it still significantly absorbs the spectrum (M22). Therefore, we need to take into account its presence in our modeling of the HETG spectra. To fit the obscurer, we adopt the model of Kaastra et al. (2014) that was derived from the large XMM-Newton campaign. In this model, the obscurer has two components, representing denser (colder) clumps embedded in a more diffuse (warmer) medium. Previous studies have found that the covering fraction ( $C_f$ ) of the warm phase is the main variable parameter (Mehdipour et al. 2016b; Cappi et al. 2016). As discussed in M22, the decline in obscuration is attributed to lowering the covering fraction of the obscurer. Therefore, we fit  $C_f$  in our modeling of the HETG spectra. Other parameters of the obscurer are kept fixed because they are not needed to be refitted, and it would be challenging to constrain them with Chandra alone.

Figure 2 shows the absorption lines that are significantly detected with HETG in the 2019 and 2022 obscured epochs. They are compared with the unobscured HETG spectrum from 2002, as well as the absorption profiles of the key UV lines from HST observations. Our measured ionic column densities using the `slab` modeling are displayed in Figure 3. In this figure, we compare what is measured from observation with the “predicted” one, which would correspond to the 2002 gas responding only to the ionizing SED in 2019 and 2022 (i.e., the deionization scenario due to shielding). The best-fit model to the HETG spectra using `pion` modeling is shown in Figure 4, and the corresponding parameters are given in Table 2. The associated SED models that we have derived for each epoch using our continuum modeling (`comt`, `pow`, and `refl` components) are shown in Figure 5. The unobscured SEDs show the intrinsic continuum, while the obscured SEDs include absorption by the obscurer. The corresponding luminosities of the SEDs are reported in Table 3. We discuss these results in the following section.

### 4. Discussion and Conclusions

In this paper, we investigated how the ionized outflow in NGC 5548 has evolved and assessed the impact of the obscurer on the ionized outflow. The decline in obscuration, and the high-energy spectral coverage of HETG, makes it possible to carry out high-resolution X-ray spectroscopy of the absorption lines to measure any changes in the parameters of the ionized outflow. The previous X-ray studies of NGC 5548 in the historical unobscured epoch have shown that its ionized outflow consists of multiple ionization and velocity components (Kaastra et al. 2014; Ebrero et al. 2016b). However, Chandra’s loss of effective area in the soft X-ray band due to the ACIS contamination means that only the high-ionization component of the outflow can be constrained in the 2019 and 2022 obscured spectra. The detection of other components at longer wavelengths is

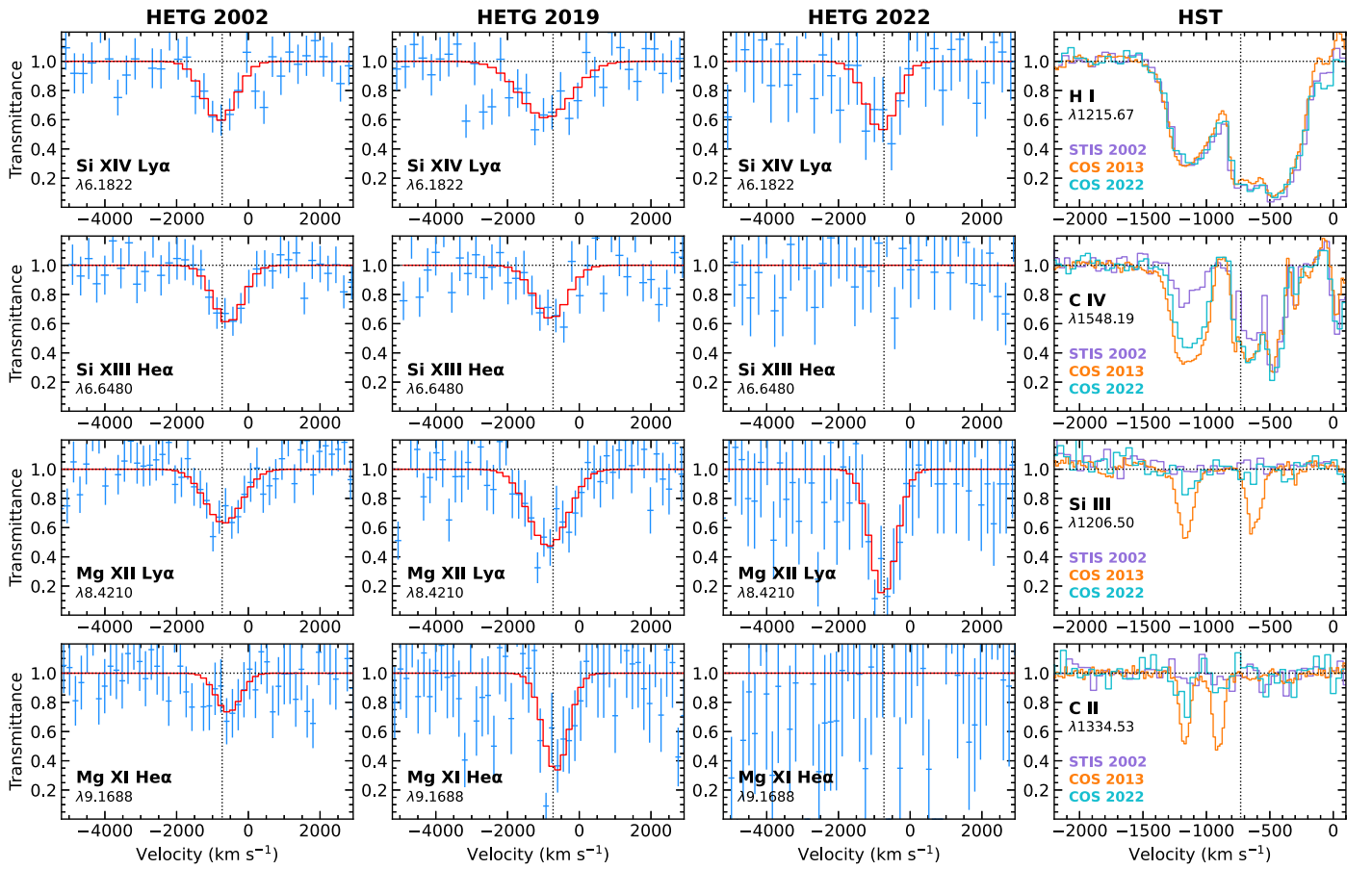


**Figure 2.** Profiles of the absorption lines in the high-resolution spectra of NGC 5548. The X-ray lines from the three epochs observed with HETG are compared in the first three columns. They are fitted with our `slab` modeling, shown in red. For comparison, the profiles of the relevant UV absorption lines from HST observations are shown in the fourth column. The dotted vertical line in all panels is drawn at a velocity of  $-730 \text{ km s}^{-1}$  for visual reference.

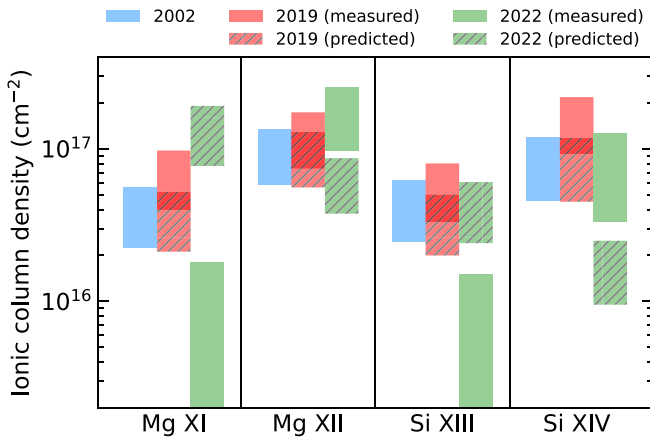


**Figure 3.** Column densities of individual ions measured via `slab` modeling of absorption lines in the HETG spectra of the three epochs. The height of each band represents the measurement uncertainty. The “predicted” values for the 2019 and 2022 epochs correspond to the deionization scenario, in which the 2002 outflow is shielded by the obscurer and thus is illuminated by the obscured SED. In the 2022 observation, the measured and predicted ionic column densities differ significantly.

nonetheless challenging due to still significant absorption of the continuum by the obscurer. The absorption lines that are most significantly detected with HETG belong to Mg XI, Mg XII, Si XIII, and Si XIV, as shown in Figure 2. We find interesting changes in the strength of these lines that we interpret here based on the results of our modeling.

#### 4.1. Impact of the Obscurer on the UV and X-Ray Components of the Ionized Outflows

Evidence for shielding (deionization) of the ionized outflows by the obscurer is seen in the HST UV spectra of NGC 5548. This was most recently discussed in M22, in which the strength of the low-ionization absorption lines follows the strength of the X-ray obscuration. This effect can be seen in the appearance of the C II and Si III lines in Figure 2, where they are strongest in 2013 (i.e., the epoch of strongest X-ray obscuration) and have become significantly weaker in 2022 (because of the lowered obscuration). In 2002, these lines are not detected, as NGC 5548 was unobscured. Interestingly, in our HETG study we find that the ionized outflow in X-rays does not follow the deionization scenario that is apparent in the UV. The results of both types of our modeling, `slab` (independent fitting of individual lines) and `pion` (photo-ionization modeling), are in agreement and support this finding.

Figure 3 shows that the ionic column density of the He-like species (Mg XI and Si XIII) became significantly lower in 2022. As shown in Table 2, this is caused by an increase in the ionization parameter  $\xi$  and the column density  $N_{\text{H}}$  of the ionized outflow compared with the 2002 unobscured epoch. This behavior is contrary to the deionization scenario, in which the shielding by the obscurer would lower the ionization of the gas. Interestingly, in the case of C IV absorption at around  $-800 \text{ km s}^{-1}$  in Figure 2 (i.e., close to the outflow velocity of the ionized outflow that is seen in X-rays), the absorption in

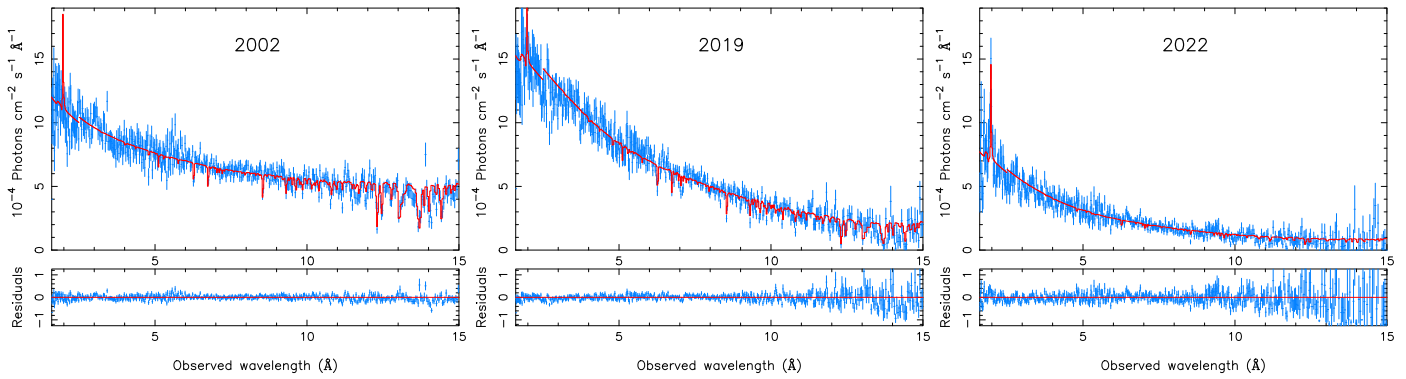


**Figure 4.** Best-fit  $\text{pion}$  model to the 2002 (left panel), 2019 (middle panel), and 2022 (right panel) HETG spectra of NGC 5548. Residuals of the fits, defined as (data – model)/model, are displayed in the bottom panels. The parameters of the  $\text{pion}$  photoionization modeling are given in Table 2, and the associated SED models are displayed in Figure 5.

**Table 2**

Best-fit Parameters of the Ionized Outflow (Warm Absorber), the Obscurer, and the Continuum Components from  $\text{pion}$  Modeling of the Three HETG Spectra

Parameter	2002	2019	2022
<b>Ionized outflow:</b>			
$\log \xi$ (erg cm s <sup>-1</sup> )	$2.46 \pm 0.02$	$2.54 \pm 0.03$	$2.96 \pm 0.05$
$N_{\text{H}}$ (10 <sup>21</sup> cm <sup>-2</sup> )	$4.0 \pm 0.3$	$5.3 \pm 0.3$	$8.0 \pm 1.0$
$v_{\text{out}}$ (km s <sup>-1</sup> )	$730 \pm 20$	730 (c)	730 (c)
$\sigma_v$ (km s <sup>-1</sup> )	$390 \pm 30$	390 (c)	390 (c)
<b>Obscurer:</b>			
$C_f$	0 (f)	$0.75 \pm 0.03$	$0.65 \pm 0.05$
<b>Continuum:</b>			
pow Norm.	$4.8 \pm 0.1$	$10.3 \pm 0.1$	$3.1 \pm 0.1$
pow $\Gamma$	$1.64 \pm 0.02$	$1.84 \pm 0.03$	$1.61 \pm 0.03$
comt Norm.	3.6 (f)	6.0 (f)	6.0 (f)
refl scale	$0.37 \pm 0.04$	0.37 (c)	0.37 (c)
C-stat/d.o.f.	5613/5122	5173/4589	4581/4158

**Note.** The normalization of the power-law component (pow) is in units of  $10^{51}$  photons s<sup>-1</sup> keV<sup>-1</sup> at 1 keV, and the normalization of the Comptonization component (comt) is in  $10^{55}$  photons s<sup>-1</sup> keV<sup>-1</sup>. The “(f)” denotes that the value of the parameter is kept fixed, and “(c)” means the parameter is coupled to another one in our modeling.

2022 is weaker than in 2013. This is most likely because the C IV absorbing gas became more ionized, similar to what is seen in the X-rays by HETG. It is worth noting that the H I Ly $\alpha$  line appears unchanged in Figure 2 because this partially covering feature is highly saturated; thus changes in the H I column density cannot produce any discernible variability in the absorption profile.

The results of our SED modeling suggest that change in the intrinsic broadband continuum is not responsible for the observed variability of the HETG absorption lines. We have derived the SED for each epoch (Figure 5 and Table 2) and carried out photoionization modeling. The observed change in the shape and luminosity of the SED (Figure 5 and Table 3) is not sufficient to induce the significant change in the ionization parameter  $\xi$  of the ionized outflow (Table 2). The parameter  $\xi$  is higher by a factor of about three in 2022 than in 2002, whereas the luminosity of the ionizing continuum is only 10% higher. Therefore, regardless of whether the unobscured or obscured SED illuminates the ionized outflow, the observed change in the X-ray absorption lines cannot be explained by the SED

variability. We note that this HETG result is also supported by the Swift X-ray and UV monitoring of NGC 5548 (M22), which shows that no significant flaring occurred near or during our observations to induce such a jump in the ionization of the gas. Interestingly, the X-ray line variability seen by HETG is in contrast to the general variability of the UV absorption lines, which predominantly follow the ionizing SED (Arav et al. 2015).

The best-fit parameters of Table 2 also indicate that the total column density  $N_{\text{H}}$  of the warm absorber increases with the ionization parameter  $\xi$  over the three epochs that we have investigated. Such a trend was previously found by Steenbrugge et al. (2003) for the historical warm absorber of NGC 5548, where  $N_{\text{H}}$  versus  $\xi$  was seen to follow a power-law distribution. This relation is thought to be a manifestation of the optical depth of the absorber being constant (Dehghanian et al. 2021).

The ionization energies for the production of the two He-like ions that have disappeared in 2022 (Mg XI and Si XIII) are in the range of 0.4–0.5 keV. This corresponds to the energy band where the ionizing SED that is transmitted by the SED is significantly diminished, as shown by the computations of Dehghanian et al. (2021). On the other hand, the ionization energies for the production of the two H-like ions (Mg XII and Si XIV) are in the higher range of 1.8–2.4 keV (Table 3), which is less affected by the obscuration. Because the obscurer absorbs a significant amount of the incident SED, it would also reemit to conserve energy (Dehghanian et al. 2021). This might imply that in 2022, the warm absorber was not illuminated by the reprocessed emission from the obscurer and was seeing only the transmitted SED, which is diminished over the 0.4–0.5 keV band. However, in the 2019 observation, the Mg XI and Si XIII lines are detected, which would imply that the warm absorber was illuminated by the reprocessed emission. The origin of this behavior between 2019 and 2022 is uncertain, but may be due to changes in the parameters of the obscurer, in particular its ionization parameter, which would alter the spectral characteristics of its reprocessed emission. However, measuring the ionization parameter of the obscurer and its changes has been extremely challenging in all previous studies and cannot be obtained from fitting the HETG spectra. As discussed in Kriss et al. (2019), because of the complex and multicomponent nature of the obscurer, finding a unique photoionization solution has not been feasible.

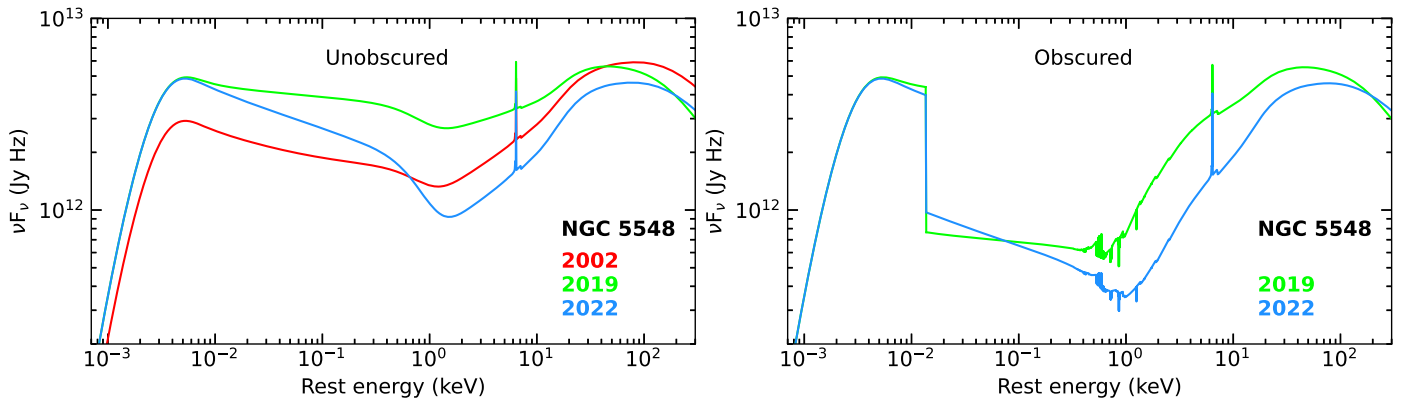


**Figure 5.** Derived SED models for the three epochs of NGC 5548. The best-fit parameters of the continuum components are provided in Table 2. The unobscured SEDs, shown in the left panel, would illuminate the obscurer. The obscured SEDs, shown in the right panel, would illuminate any outflow that is farther out and shielded by the obscurer. The luminosities of these unobscured and obscured SEDs are given in Table 3.

**Table 3**

Luminosities of the Unobscured and Obscured SEDs of NGC 5548 (Figure 5) for the Three Epochs

	2002	2019	2022
Unobscured SED:			
$L_{1-1000}$	0.9	1.6	1.0
$L_{\text{bol}}$	2.5	3.4	2.6
Obscured SED:			
$L_{1-1000}$	...	0.6	0.4
$L_{\text{bol}}$	...	2.3	2.0
$L_{\nu}$ ratio at ionization potential:			
H I (13.60 eV)	...	0.17	0.25
C II (24.38 eV)	...	0.17	0.25
C IV (64.49 eV)	...	0.17	0.25
Mg XI (1761.80 eV)	...	0.52	0.54
Mg XII (1962.66 eV)	...	0.54	0.57
Si III (33.49 eV)	...	0.17	0.25
Si XIII (2437.66 eV)	...	0.64	0.66
Si XIV (2673.18 eV)	...	0.67	0.68

**Note.**  $L_{1-1000}$  corresponds to the 1–1000 Ryd ionizing luminosity and  $L_{\text{bol}}$  to the total bolometric luminosity of the SED. The luminosities are in units of  $10^{44}$  erg  $\text{s}^{-1}$ . The  $L_{\nu}$  ratio corresponds to the obscured versus unobscured specific luminosity ratio at the energy of the ionization potential of an ion.

#### 4.2. Interpretation of the Variability of the HETG X-Ray Absorption Lines

The study of historical unobscured spectra by Ebrero et al. (2016b) derived constraints for the location of various components of the ionized outflows in NGC 5548. Their component E is the one that matches most closely our model in terms of  $\xi$  and outflow velocity. They found the distance of this component from the black hole is  $0.6 < R < 2.2$  pc. We suggest the obscuring wind itself is unlikely to have reached such distances to make a direct contribution to the observed HETG absorption lines. The earliest available evidence for the obscurer comes from the Swift observation of 2012 February (Mehdipour et al. 2016b) in the X-ray band and the HST observation of 2011 June in the UV band (Kaastra et al. 2014). This is about 11 yr before our 2022 HETG observation. The precise time for a potentially earlier appearance of the obscurer is not known because of lack of regular monitoring prior to 2012; however, the 2007 August Swift observation is unobscured (Mehdipour et al. 2016b). Therefore, the maximum

possible travel time for the obscurer before our 2022 HETG observation is about 14.5 yr. The outflow velocity of the obscurer according to the broad UV absorption lines is dominant at around  $2000 \text{ km s}^{-1}$ , reaching up to  $5000 \text{ km s}^{-1}$  (Kaastra et al. 2014; Kriss et al. 2019). With this velocity range, the obscurer would have traveled a distance of 27–67 light-days (0.02–0.06 pc) over 11 yr, or potentially a maximum distance of 35–88 light-days (0.03–0.07 pc) over 14.5 yr. These distances correspond to the outer BLR rather than the NLR and the estimated location of  $0.6 < R < 2.2$  pc by Ebrero et al. (2016b).

The HETG absorption lines are significantly narrower (few  $100 \text{ km s}^{-1}$ ) than the broad UV lines (few  $1000 \text{ km s}^{-1}$ ) that are associated with the obscurer in the vicinity of the BLR. Also, the outflow velocity of the HETG absorption lines shows no significant change among the three epochs, again suggesting that the obscurer is not directly contributing to these lines. The absorption lines in the 2002 and 2019 epochs have similar strengths, whereas they show key differences between 2019 and 2022 (Figure 2). This points to variability on shorter timescales than the decadal timescale of the evolution of the obscurer.

The most plausible explanation for the observed line variability may be due to the orbital motion of the warm-absorber outflow as it traverses our line of sight. At a distance of  $0.6 < R < 2.2$  pc (Ebrero et al. 2016b), the Keplerian velocity would range from  $370$  to  $710 \text{ km s}^{-1}$  for NGC 5548’s black hole mass of  $7 \times 10^7 M_{\odot}$  (Horne et al. 2021). This orbital velocity range is consistent with our measured velocity dispersion of  $390 \text{ km s}^{-1}$ , as well as with the outflow velocity of  $730 \text{ km s}^{-1}$  (Table 2 and Figure 2). Adopting a fiducial X-ray source size (diameter) of  $20$  gravitational radii  $GM/c^2$ , the crossing time with the Keplerian velocity would be 15–30 days. Therefore, on the longer timescales that we are probing with our three observations (2002, 2019, and 2022), the absorbing gas can feasibly be replaced by new material. In the likely case of this gas being inhomogeneous and clumpy, as it moves, variations in the ionization parameter and the column density are expected, as seen in our HETG observations.

The results of this study highlight the complex relation between the obscurer and the ionized outflows in NGC 5548. Although some of the more distant outflows in the UV appear to be shielded, the more ionized outflow that is seen in X-rays with HETG is not significantly affected by the obscurer. In addition, the shielding has a greater impact on the population of

the low-ionization UV ions that is more dramatic than the high-energy species seen with the HETG due to the higher optical depth of the obscurer at their relevant ionization edges. This can be seen by the obscured versus unobscured specific luminosity ratio at the ionization potential of each ion (Table 3). It is not certain to what extent the origin and geometry of the obscurer and the warm-absorber outflow play a role. For instance, if the obscurer is launched from the disk and mainly moves in polar directions as a result of being magnetically driven (Fukumura et al. 2017), it might not effectively shield regions in the equatorial directions, where the warm-absorber outflow (Component E of Ebrero et al. 2016b) may originate with material evaporated from the torus. Thus, in such a case the obscurer and the ionized outflow would operate and vary independently from each other. On the other hand, if the obscurer and the warm-absorber outflow share a common origin and launching mechanism, one would expect some degree of observable correlation between their variability behaviors. Furthermore, the variable and patchy nature of the obscurer may play a role by letting through various ionizing SEDs that would illuminate the warm absorber, causing short-term changes in the ionization of the warm absorber, as seen in the 2019 and 2022 epochs.

The potential role of X-ray shielding in radiation-driven winds is open for further research. The hydrodynamical simulation study of Higginbottom et al. (2014) finds that the shielding may not be effective in keeping the outer UV absorber from being over-ionized because of reprocessing and scattering of the ionizing X-rays. Also, the study of broad absorption line quasars by Luo et al. (2014) suggests that they are intrinsically X-ray faint and do not need shielding to drive winds. With HETG we are only able to probe the highest ionization component of the warm-absorber outflow, and our findings suggest that it is not significantly shielded by the obscurer. The recently launched XRISM/Resolve microcalorimeter (XRISM Science Team 2020), alongside XMM-Newton's Reflection Grating Spectrometer, presents a unique opportunity to probe all the X-ray components of the outflow in NGC 5548 as obscuration further evolves over the coming years.

### Acknowledgments

Support for this work was provided by the National Aeronautics and Space Administration through Chandra Award Number 23103X issued by the Chandra X-Ray Center, which is operated by the Smithsonian Astrophysical Observatory for and on behalf of the National Aeronautics and Space Administration under contract NAS8-03060. This work was also supported by NASA through a grant for HST program number 16842 from the Space Telescope Science Institute, which is operated by the Association of Universities for Research in Astronomy, Incorporated, under NASA contract NAS5-26555. SRON is supported financially by NWO, the Netherlands Organization for Scientific Research. We thank the anonymous referee for the constructive comments.

*Facilities:* NASA Chandra X-ray Observatory (CXO) Satellite Mission, HST

### ORCID iDs

Missagh Mehdipour  <https://orcid.org/0000-0002-4992-4664>  
 Gerard A. Kriss  <https://orcid.org/0000-0002-2180-8266>  
 Jelle S. Kaastra  <https://orcid.org/0000-0001-5540-2822>  
 Elisa Costantini  <https://orcid.org/0000-0001-8470-749X>  
 Liyi Gu  <https://orcid.org/0000-0001-9911-7038>  
 Hermine Landt  <https://orcid.org/0000-0001-8391-6900>  
 Junjie Mao  <https://orcid.org/0000-0001-7557-9713>  
 Daniele Rogantini  <https://orcid.org/0000-0002-5359-9497>

### References

- Arav, N., Chamberlain, C., Kriss, G. A., et al. 2015, *A&A*, 577, A37  
 Cappi, M., De Marco, B., Ponti, G., et al. 2016, *A&A*, 592, A27  
 de Vaucouleurs, G., de Vaucouleurs, A., Corwin, Herold, G. J., et al. 1991, Third Reference Catalogue of Bright Galaxies (New York: Springer)  
 Dehghanian, M., Ferland, G. J., Kriss, G. A., et al. 2019a, *ApJ*, 877, 119  
 Dehghanian, M., Ferland, G. J., Peterson, B. M., et al. 2019b, *ApJL*, 882, L30  
 Dehghanian, M., Ferland, G. J., Peterson, B. M., et al. 2021, *ApJ*, 906, 14  
 Di Gesu, L., Costantini, E., Ebrero, J., et al. 2015, *A&A*, 579, A42  
 Ebrero, J., Kriss, G. A., Kaastra, J. S., & Ely, J. C. 2016a, *A&A*, 586, A72  
 Ebrero, J., Kaastra, J. S., Kriss, G. A., et al. 2016b, *A&A*, 587, A129  
 Fukumura, K., Kazanas, D., Shrader, C., et al. 2017, *NatAs*, 1, 0062  
 Gaspari, M., & Sądowski, A. 2017, *ApJ*, 837, 149  
 Gaspari, M., Tombesi, F., & Cappi, M. 2020, *NatAs*, 4, 10  
 Harrison, C. M., Costa, T., Tadhunter, C. N., et al. 2018, *NatAs*, 2, 198  
 Higginbottom, N., Proga, D., Knigge, C., et al. 2014, *ApJ*, 789, 19  
 Horne, K., De Rosa, G., Peterson, B. M., et al. 2021, *ApJ*, 907, 76  
 Kaastra, J. S., Kriss, G. A., Cappi, M., et al. 2014, *Sci*, 345, 64  
 Kaastra, J. S., Mewe, R., Liedahl, D. A., Komossa, S., & Brinkman, A. C. 2000, *A&A*, 354, L83  
 Kaastra, J. S., Mewe, R., & Nieuwenhuijzen, H. 1996, in *UV and X-ray Spectroscopy of Astrophysical and Laboratory Plasmas*, ed. K. Yamashita & T. Watanabe (Tokyo: Univ. Academy Press), 411  
 Kaastra, J. S., Raassen, A. J. J., de Plaa, J., & Gu, L. 2022, SPEX X-ray spectral fitting package v3.07.01, Zenodo, doi:10.5281/zenodo.7037609  
 Kara, E., Mehdipour, M., Kriss, G. A., et al. 2021, *ApJ*, 922, 151  
 King, A., & Pounds, K. 2015, *ARA&A*, 53, 115  
 Kriss, G. A., De Rosa, G., Ely, J., et al. 2019, *ApJ*, 881, 153  
 Kynoch, D., Landt, H., Dehghanian, M., Ward, M. J., & Ferland, G. J. 2022, *MNRAS*, 516, 4397  
 Laha, S., Reynolds, C. S., Reeves, J., et al. 2021, *NatAs*, 5, 13  
 Loders, K., Palme, H., & Gail, H. P. 2009, *LanB*, 4B, 712  
 Longinotti, A. L., Krongold, Y., Kriss, G. A., et al. 2013, *ApJ*, 766, 104  
 Luo, B., Brandt, W. N., Alexander, D. M., et al. 2014, *ApJ*, 794, 70  
 Mao, J., Kriss, G. A., Landt, H., et al. 2022, *ApJ*, 940, 41  
 Mehdipour, M., Kaastra, J. S., & Kallman, T. 2016a, *A&A*, 596, A65  
 Mehdipour, M., Kaastra, J. S., Kriss, G. A., et al. 2016b, *A&A*, 588, A139  
 Mehdipour, M., Kaastra, J. S., Kriss, G. A., et al. 2015, *A&A*, 575, A22  
 Mehdipour, M., Kaastra, J. S., Kriss, G. A., et al. 2017, *A&A*, 607, A28  
 Mehdipour, M., Kriss, G. A., Costantini, E., et al. 2022, *ApJL*, 934, L24  
 Mehdipour, M., Kriss, G. A., Kaastra, J. S., et al. 2021, *A&A*, 652, A150  
 Miller, J. M., Kaastra, J. S., Miller, M. C., et al. 2015, *Natur*, 526, 542  
 Proga, D., & Kallman, T. R. 2004, *ApJ*, 616, 688  
 Schlegel, D. J., Finkbeiner, D. P., & Davis, M. 1998, *ApJ*, 500, 525  
 Serafinelli, R., Braito, V., Severgnini, P., et al. 2021, *A&A*, 654, A32  
 Silk, J., & Rees, M. J. 1998, *A&A*, 331, L1  
 Steenbrugge, K. C., Kaastra, J. S., Crenshaw, D. M., et al. 2005, *A&A*, 434, 569  
 Steenbrugge, K. C., Kaastra, J. S., de Vries, C. P., & Edelson, R. 2003, *A&A*, 402, 477  
 Wakker, B. P., Lockman, F. J., & Brown, J. M. 2011, *ApJ*, 728, 159  
 Wildy, C., Landt, H., Ward, M. J., Czerny, B., & Kynoch, D. 2021, *MNRAS*, 500, 2063  
 XRISM Science Team 2020, arXiv:2003.04962